# Supplementary Information for

## Ginkgo seed shell provides a unique model for bioinspired design

Yuanyuan Zhang[1,4†], Jiajun Mao[1†], Jingsong Peng[1†], Antoni P. Tomsia[1], Lei Jiang[1,2], Qunfeng Cheng[1,3*]

[1]School of Chemistry, Key Laboratory of Bio-inspired Smart Interfacial Science and Technology of Ministry of Education, Beihang University; Beijing 100191, P. R. China.

[2]Key Laboratory of Bio-inspired Materials and Interfacial Science, Technical Institute of Physics and Chemistry, Chinese Academy of Sciences; Beijing 100190, P. R. China.

[3]School of Materials Science and Engineering, Zhengzhou University, Zhengzhou 450001, P. R. China

[4]School of Chemistry and Chemical Engineering, Inner Mongolia University, Hohhot 010021, P. R. China

†These authors contributed equally to this work.

*Corresponding author: Qunfeng Cheng
**Email:** cheng@buaa.edu.cn

**This PDF file includes:**

- Supplementary text
- Figures S1 to S22
- Table S1
- Legends for Movies S1 to S2
- SI References

**Other supplementary materials for this manuscript include the following:**

- Movies S1 to S2

**Supplementary Information Text**

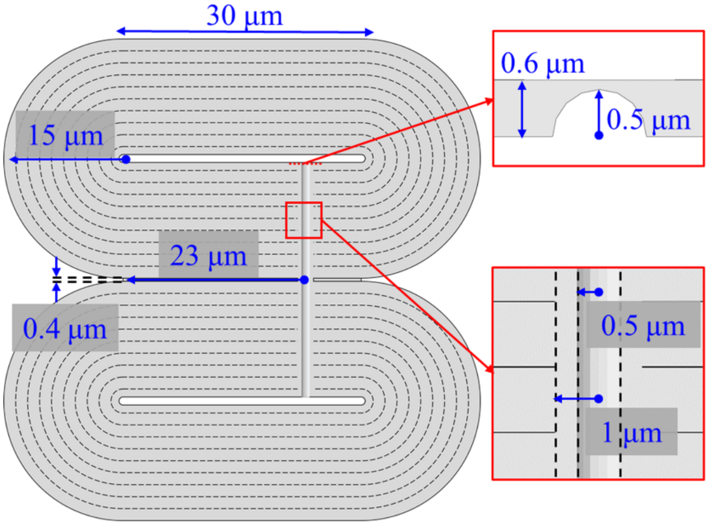


**Scheme S1.** The 2D finite element model of adjacent sclereids.

**Calculation of Young's modulus**

Nanoindentation tests can be performed in either load-controlled or displacement-controlled feedback mode. Here we used the load-controlled mode. A test is performed by applying a force to drive an indenter probe into the sample surface and then reducing the force to withdraw the probe. The applied load (*P*) and indenter displacement (*h*) into the sample are continuously monitored. A load vs. displacement curve can then be generated from the collected data. Scheme S2 depicts an example of a load vs. displacement curve in which the load is increased at a constant rate to some peak value (loading), held at that value for a set amount of time, and then decreased to zero (unloading). The sample hardness (*H*) and reduced elastic modulus ($E_r$) can then be calculated from the curve.

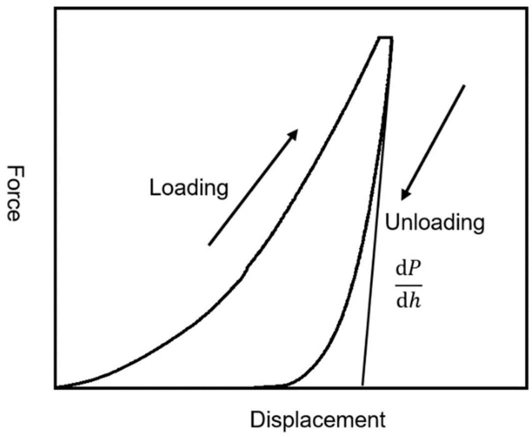


**Scheme S2.** Example of a force versus displacement curve from an indentation test on ginkgo seed shell.

Reduced modulus is calculated from nanoindentation. The reduced modulus is defined by the equation

$$E_r = \frac{S\sqrt{\pi}}{2\sqrt{A}} \quad (1)$$

where *S*, the unloading stiffness, is defined by

$$S = \frac{dP}{dh} \quad (2)$$

and *A* is the projected contact area.

The reduced modulus is related to the modulus of elasticity ($E_s$) through the equation

$$\frac{1}{E_r} = \frac{(1-v_i^2)}{E_i} + \frac{(1-v_S^2)}{E_s} \quad (3)$$

Where the subscript *i* corresponds to the indenter material, the subscript *s* refers to the indented sample material, and *v* is Poisson's ratio. For a diamond indenter probe, $E_i$ is 1140 GPa and $v_i$ is 0.07. Poisson's ratio varies between 0 and 0.5 for most materials (the Poisson's ratio we used here is 0.3).

The unloading stiffness (*S*) is calculated by fitting the unloading curve to the power law relation

$$P = A\left(h - h_f\right)^m \quad (4)$$

where *A*, $h_f$, and m are arbitrary fitting parameters. The stiffness at the peak of the unloading curve represents the elastic response of the material at the initial point of unloading, which can be calculated from the derivative of equation 4, evaluated at $h = h_{max}$.

$$S = \frac{dP}{dh}\Big|_{h=h\max} = mA(h_{\max} - h_f)^{m-1} \quad (5)$$

The hardness is defined by the ratio of the maximum load to the projected contact area, or

$$H = \frac{p_{\max}}{A} \quad (6)$$

The contact area, *A*, is a function of the probe's contact depth, $h_c$. The area function *A* ($h_c$) is unique for each probe and is determined through a calibration on a reference material. The contact depth is calculated from the load vs. displacement curve as

$$h_c = h_{\max} - \varepsilon \frac{p_{\max}}{S} \quad (7)$$

Equation 7 accounts for the fact that the contact depth is always less than the peak displacement due to the deflection of the surface around the contact perimeter. $\varepsilon$ is a geometric constant taken to be 0.75 for most common probe geometries. The average modulus was obtained from seven ginkgo samples.

The fracture toughness and the crack extension resistance curve (R-curve) were determined to evaluate the toughening behavior of the natural seed shell. Three-point bend tests were performed to generate stress-strain information with a support span of 3.5 mm on the Gatan Microtest 2 kN three-point bend stage at a displacement rate of 0.033 mm/min. The plane-strain fracture toughness, $K_{IC}$, and R-curve measurements were performed on the single-edge notched beam.

The converted stress intensity factor $K_{JC}$ is determined in terms of

$$K_{JC} = \sqrt{\left(J_{el} + J_{pl}\right) \times E'} \quad (8)$$

where $J_{el}$ is the elastic component of *J*-integral, $J_{pl}$ the plastic component, and *E′* is calculated from

$$E' = \frac{E}{1 - \nu^2} \quad (9)$$

for plane-strain conditions, where $E$ is the elastic modulus and $v$ Poisson's ratio.

The calculation of $J_{el}$ is given by

$$J_{el} = \frac{K_{IC}^2}{E'} \quad (10)$$

where $K_{IC}$ is the plane-strain fracture toughness at or near the onset of crack initiation. $K_{IC}$ is based on the relation

$$K_{IC} = \frac{PS}{4BW^{\frac{3}{2}}} f\left(\frac{a}{W}\right) \quad (11)$$

$$f\left(\frac{a}{W}\right) = \left(7.31 + 0.21\sqrt{\frac{S}{W} - 2.9}\right)\sec\left(\frac{\pi a}{2W}\right)\sqrt{\tan\left(\frac{\pi a}{2W}\right)} \quad (12)$$

where $P$ is the applied load, $S$ the support span, $B$ the width of the specimen, $W$ the thickness, and $a$ the initial crack length. The initial crack length $a$ is equal to the depth of the notch for tested specimens.

The plastic component $J_{pl}$ is given in terms of

$$J_{pl} = \frac{2A_{pl}}{B(W - a)} \quad (13)$$

where $A_{pl}$ is the area of the plastic region under the load-displacement curve.

The crack length was measured by acquiring a movie of the in-situ three-point bend test of the samples. The real-time measurements permitted evaluation of the load-displacement curve.

**Calculation of fibril angle**

Samples for TEM were dehydrated in mixture of ethanol and acetone and then embedded in araldite. An ultramicrotome (Leica EM UC7) with a diamond knife was used to obtain ultrathin sections. The sectioned ginkgo seed shell samples were pictured with a Bruker MultiMode 8-HR both in ScanAsyst mode and tapping mode. The silicon probe (OTESPA-R3) used in the test has a nominal spring constant of 26 N/m and approximate tip apex diameter of 7 nm. Calibration has been implemented via Sader method before each experiment. Nanoindentation experiments were measured with the same probe under ScanAsyst mode.

The indentation modulus, $M$, is obtained from the slope of the unloading curve. The $S$ based on the reported by Vlassak et al. can be characterized by

$$S = dF / dU = \frac{2}{\sqrt{\pi}} M \sqrt{Ac} \quad (14)$$

where $F$ is the load, $U$ is the vertical movement of the probe, and $A_C$ is the projected contact area. Swadener and Pharr showed that the calculation of the contact area $A_C$ is written as

$$Ac = 2\pi RUc \quad (15)$$

where $R$ is the radius of the probe, and $U_C$ is the average contact depth. The value of $U_C$ can be analyzed from the Oliver–Pharr method and is given by

$$Uc = U\max - \varepsilon \frac{F\max}{S} \quad (16)$$

Next, we characterized the material properties on account of the measured indentation modulus. The microfiber is regarded as a transversely isotropic object with stiffness tensor Cijkl and has definition in a Cartesian coordinate system ($x_1$, $x_2$, $x_3$), where $x_1$ is defined along the axial direction of the microfibers, while $x_2$ and $x_3$ lie in the direction perpendicular to microfibers (Scheme S3). Especially, $x_3$ lies in the plane of the transverse section independent of the microfibril angle.

The unit normal vector is defined as n in the direction parallel to the axis of the sclereid cell. To estimate relation of the microfibers and indentation modulus, the method proposed by Vlassak et al. is employed. The indentation modulus is determined in two steps:

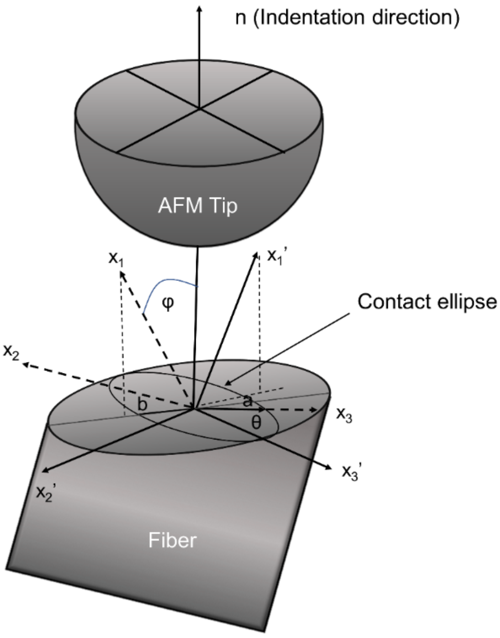


**Scheme S3.** Conical indentation in fibers and right-hand coordinate system used for the contact mechanics analysis.

The first step is according to the surface Green's function proposed by Barnett and Lothe. Upon the unit normal vector parallel to the axis, the displacement of a point *P* at a position *r* on the surface is written as

$$w(y) = \frac{1}{8\pi^2 |y|}\left[ n_k B_{km}^{-1}\left(\frac{y}{|y|}\right) nm \right] = \frac{h(\theta)}{r} \tag{17}$$

where *y* is the position vector of from *P* to *Q*, the unit vector is composed of $n_k$, and h and r are the polar coordinates of P in a coordinate system centered on *Q*. *h(θ)* is part of the surface Green's function not dependent on the angle. *B* is a second-order tensor; its components are given by

$$B_{js}(x'_3) = B_{sj}(x'_3) = \frac{1}{8\pi^2}\int_0^{2\pi} \left[ (x'_1\, x'_1)_{js} - (x'_1\, x'_2)_{jk} (x'_2\, x'_2)_{kr} (x'_2\, x'_1)_{rs} \right] d\varphi \tag{18}$$

where $x'_3$ is the normalized form of *y*. $x'_1$; $x'_2$; $x'_3$ form a right-hand coordinate system, and *φ* is the angle between vector $x'_1$ and the surface.

Barber's theory is used in the second step to establish the connection between load F and penetration *U*. The integral of conical tip shapes is flat punch pressure distribution carrying on the contact area and the deformation under the indenter. Here, we assume that this shape is an elliptical contact area, this integral for conical tip shapes is determined by major axis a and minor axis b, and the relation between force *F* and penetration *U* is given by

$$F(e, \Phi) = \frac{U^2}{\cot\gamma\alpha(e, \Phi)E(e)}' \tag{19}$$

where $\gamma$ is the cone angle and $e = \sqrt{1-(b^2/a^2)}$ is the eccentricity of the contact ellipse. The angle between major axis of the ellipse and the h for reference direction is $\Phi$, and $E(e)$ is the entire elliptic integral. *a* is obtained as

$$\alpha(e,\Phi) = \int_0^{\pi} \frac{h(\theta+\Phi)}{\sqrt{1-e^2\cos^2\theta}} d\theta \qquad (20)$$

The indentation modulus according to Barber's theory is then given as the derivative of *F* with respect to *U*, writing as

$$S = \frac{dF}{dU} = \frac{2}{\sqrt{\pi}}\sqrt{Ac}\,\frac{1}{\alpha(e,\Phi)(1-e^2)^{1/4}} \qquad (21)$$

So the indentation modulus of a cone in an anisotropic half space is reading as

$$M = \frac{1}{\alpha(e,\Phi)(1-e^2)^{1/4}} \qquad (22)$$

The relation between the indentation modulus, indentation direction, and stiff properties of the transversely isotropic cell wall materials is given by the final equation.

In order to eliminate the difference between theoretical parameters and measured value, we used the relative indentation modulus

$$R_M = \frac{M - M_{\min}}{M_{\max} - M_{\min}} \qquad (23)$$

where $M_{\min}$ represents the minimum indentation modulus within a cycle when the angle is equal to 0 degree and $M_{\max}$ represents the maximum value when the angle is equal to 90 degrees.

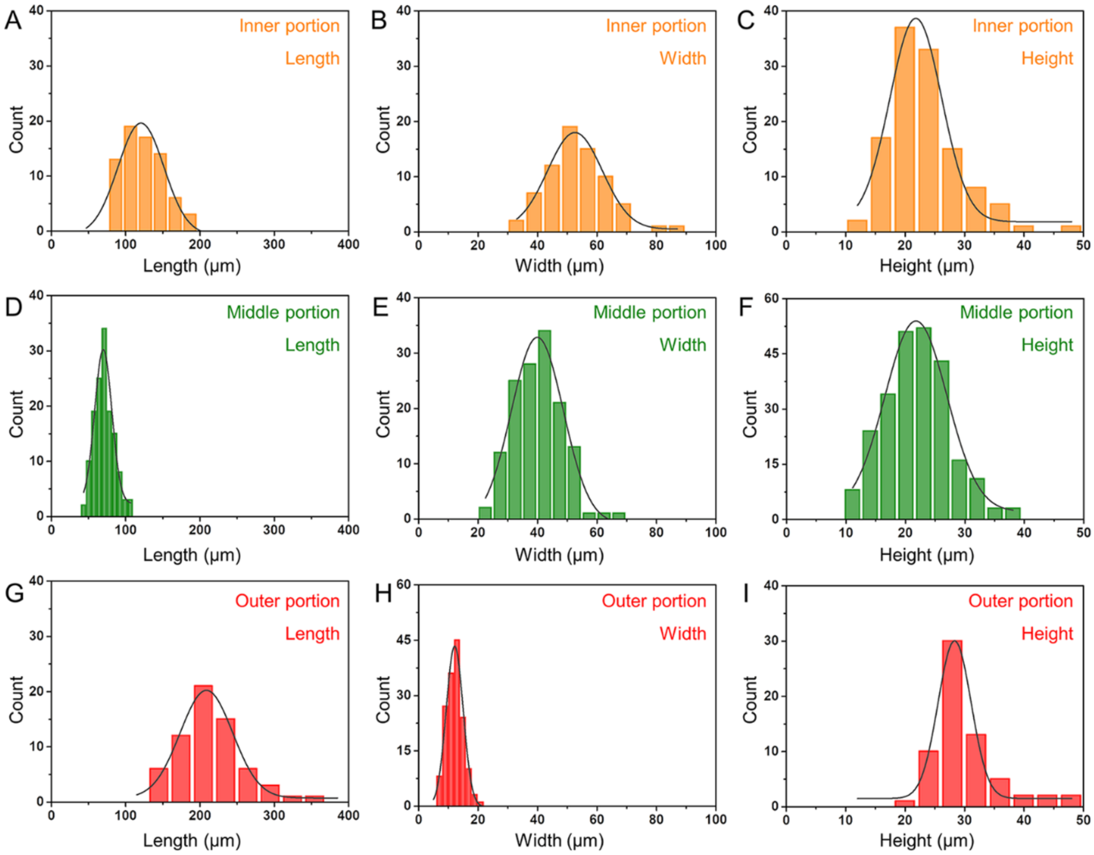


**Fig. S1. The statistical data of the size of the sclereid from the outer surface to the inner surface along the *R* direction.**

The orange graphs show the length (124.9 ± 27.6 μm) (**A**), width (53.2 ± 9.9 μm) (**B**), and height (23.4 ± 6.1 μm) (**C**) of the sclereid in the inner portion. The green graphs show the length (71.2 ± 13.23 μm) (**D**), width (40.2 ± 8.0 μm) (**E**), and height (22.0 ± 5.6 μm) (**F**) of the sclereid in the middle portion. The red graphs show the length (214.2 ± 43.6 μm) (**G**), width (12.2 ± 2.8 μm) (**H**), and height (30.2 ± 5.7 μm) (**I**) of the sclereid in the outer portion. The average aspect ratio of the three portions is 5.3, 3.2, and 17.6 of the inner portion, middle portion, and the outer portion, respectively. The outer portion accounts for only 9% of the thickness of the whole seed shell. We therefore focused mainly on the inner and middle portions of the seed shell and considered the seed shell a weakly anisotropic material with a low aspect ratio of only 3.2–5.3.

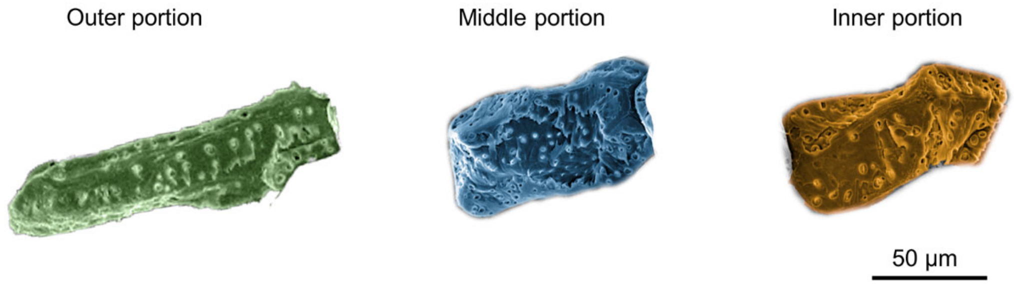


**Fig. S2. Cell types on the basis of X-ray micro-tomography and SEM images.**
The outer portion of ginkgo seed shells is composed mainly of elongated sclereids. In the middle and inner portion, more equiaxed sclereids make up the majority of the shell.

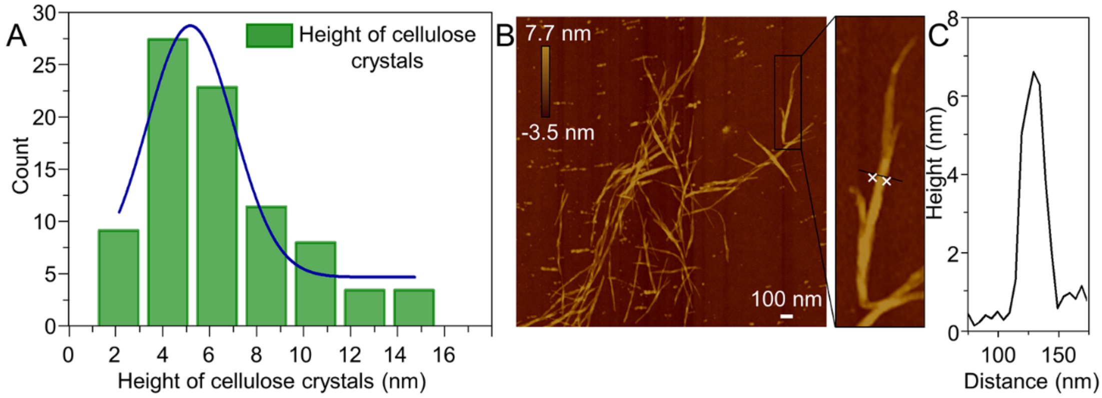


**Fig. S3. The statistical data of the height of cellulose crystals.**

The cellulose crystals were obtained from delignified ginkgo seed shell. The delignified seed shell was exfoliated by $H_2SO_4$ solution to generate the cellulose crystals. (**A**) The number-average height of cellulose crystals is deduced as 5–7 nm. (**B**) The height image of cellulose crystals. (**C**) Cross-sectional profiles obtained from AFM images.

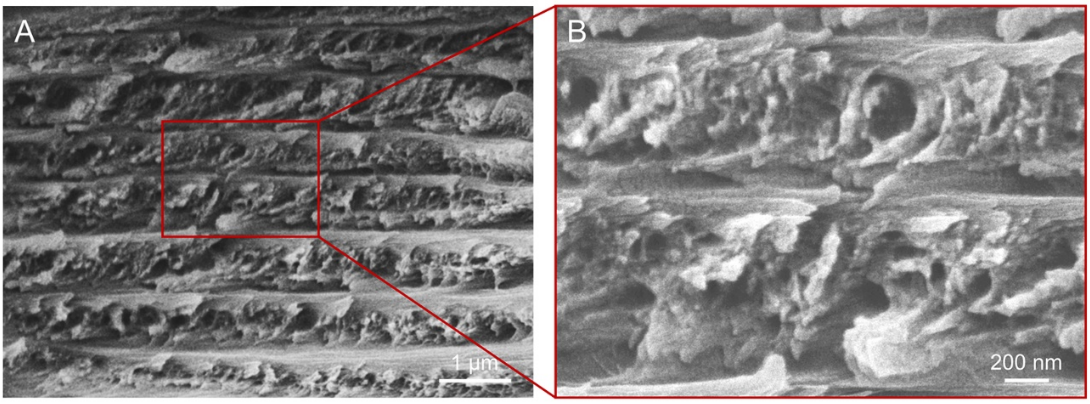


**Fig. S4. SEM images of cell walls.**

SEM images of the cell wall in a sclereid (**A**) and morphology of a sclereid with higher magnification in a manner of helicoidal arrangement (**B**). To make up the helicoidal cell wall, the cellulose microfibrils are aligned parallel into a layer, and these layers are further stacked and rotated around the normal direction. The cross section of the cell wall shows different angles between the cellulose microfibrils due to gradually varied orientation of cellulose microfibrils at different layers.

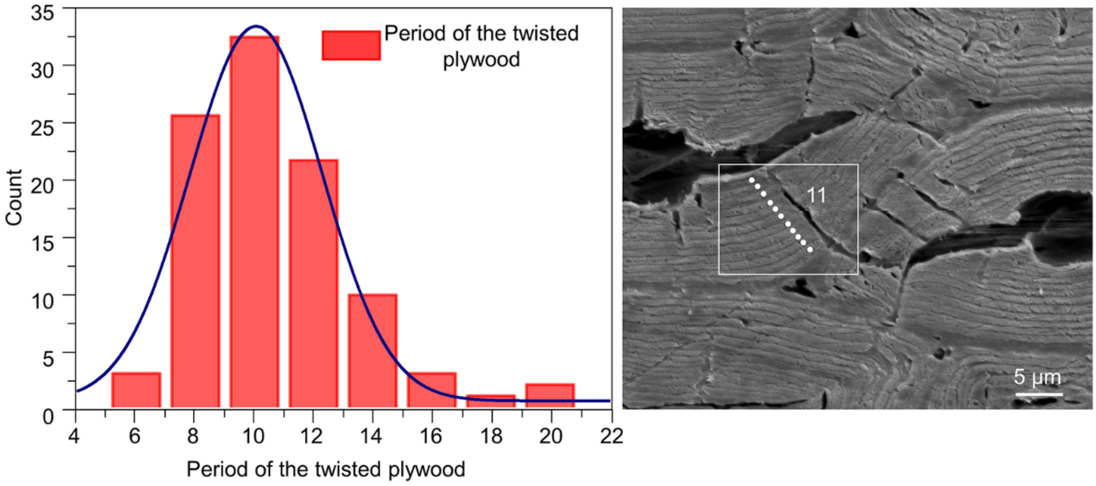


**Fig. S5. The statistical data of the period of the helicoidal layers.**

The number-average period of the helicoidal layers is deduced as 8 to 12. The corresponding SEM image shows a region of cell wall with a period of 11.

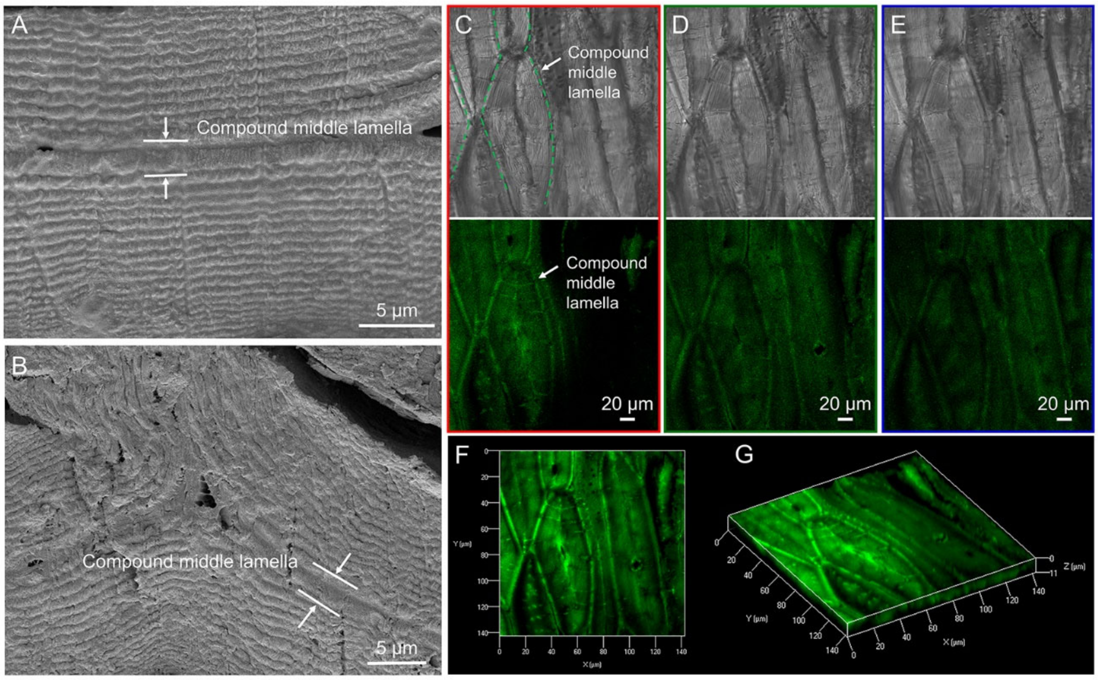


**Fig. S6. SEM images of the CML.**

(**A**, **B**) The compound middle lamella shows a thickness of several micrometers. The confocal microscopy images under bright field and corresponding fluorescent images (**C**, **D**, and **E**). (C, D) and (E) show a single optical section and (**F**) is the maximum projection. (**G**) The 3D reconstruction image of the cross section of ginkgo seed shell. This compound middle lamella includes the middle lamella, the primary cell wall, and some outer portions of the secondary cell wall. The lignin content of the compound middle lamella and the pits is much higher than that of the inner cell wall. The high content of lignin in the compound middle lamella and the pits is illustrated by the higher fluorescent intensity on the confocal images.

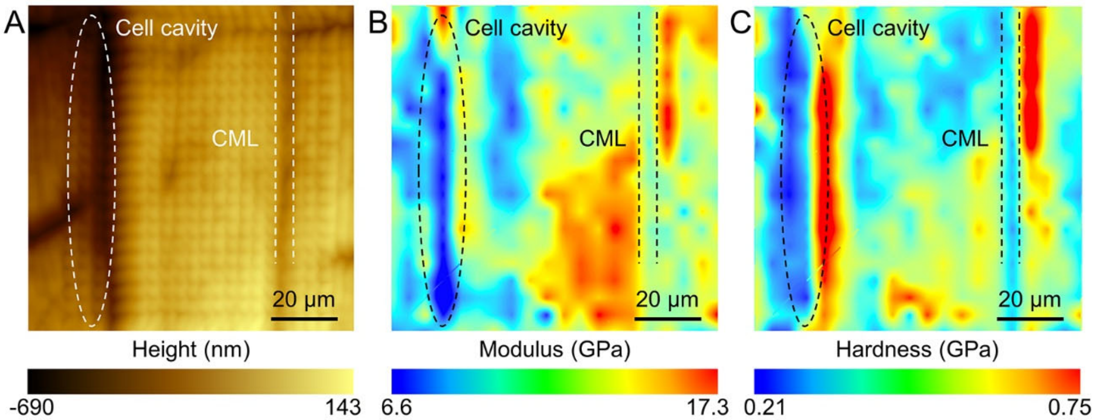


**Fig. S7. Indentation modulus and hardness of the cell unit.**
(**A**) AFM height images of the cell unit. AFM heat maps of the internal mechanical properties of the cell unit; (**B**) and (**C**) are indentation modulus and hardness, respectively.

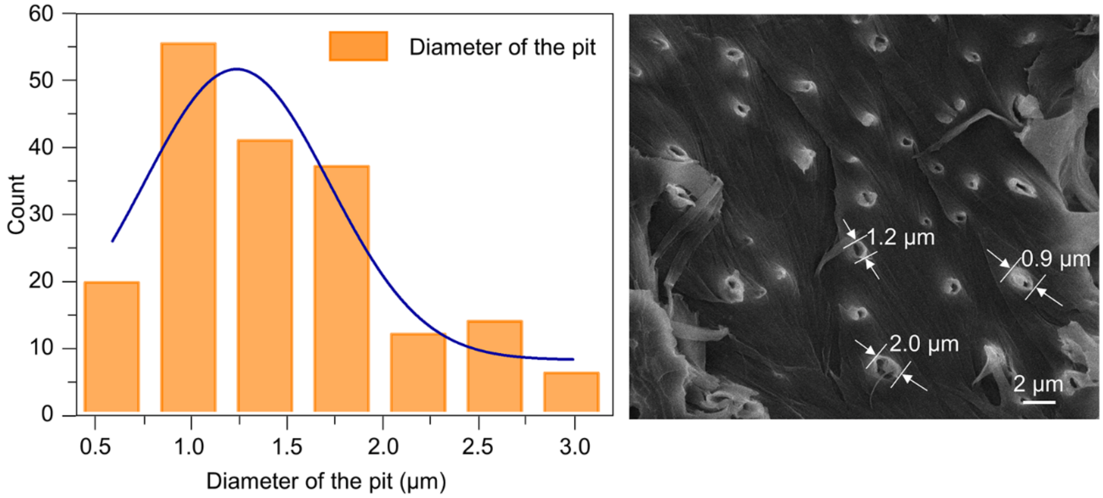


**Fig. S8. The statistical data of the diameter of the pit structure.**

The number-average diameter of the pit is deduced as 1.2 μm. The SEM image of the surface from a sclereid with fractured pits shows how the diameter of corresponding pits is measured.

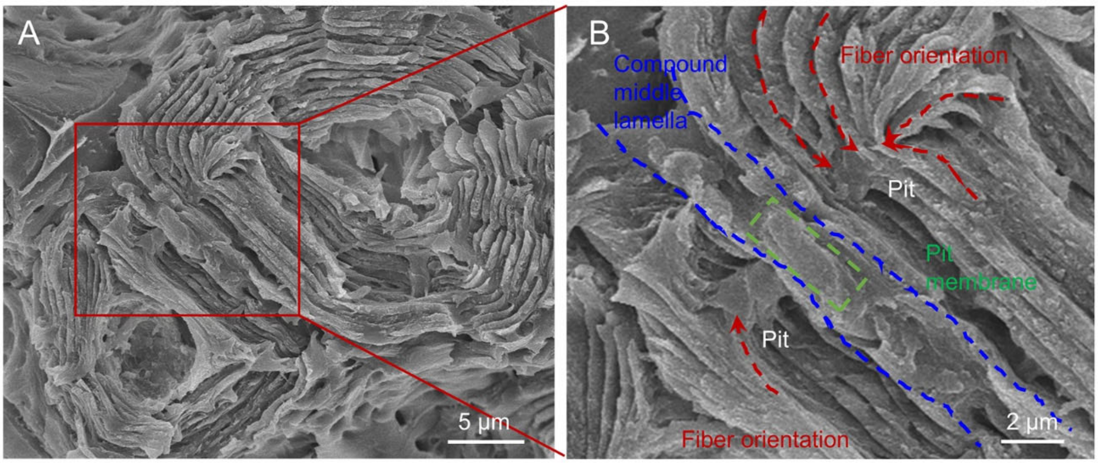


**Fig. S9. SEM images of the compound middle lamella of two adjacent sclereids cutting along the R direction.**

(**A**-**B**) The detailed morphology of the pit pair at the compound middle lamella. The dashed red arrows illustrate the orientation of these cellulose microfibrils. The dashed green areas and blue areas are the pit membrane and CML, respectively. In the junction of a pit pair, the microfibrils are oriented together to form a membrane, bonding strongly the two pits from adjacent sclereids.

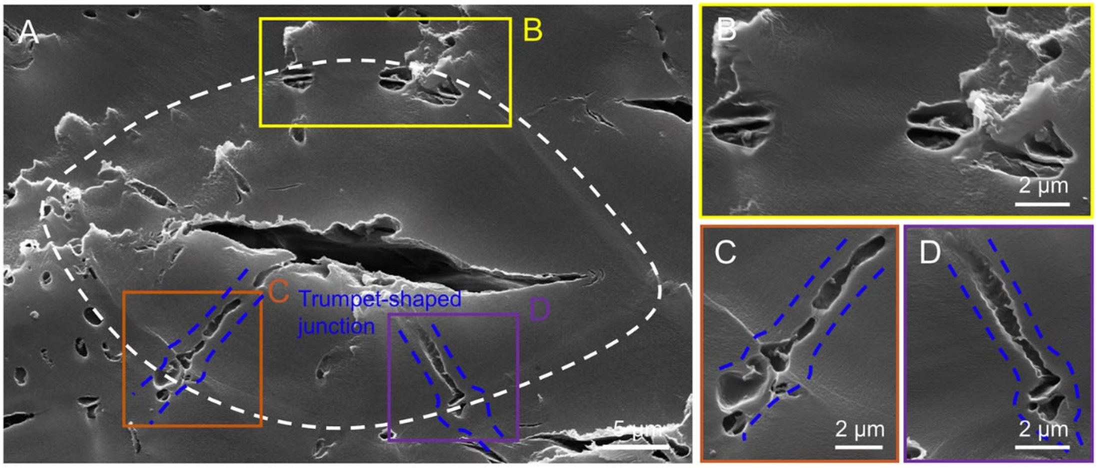


**Fig. S10. SEM image of the cross section of a polished sclereid**.

(**A**) SEM image of the cross section of a sclereid polished by ion beam milling cutting along the R direction. (**B**–**D**) SEM images with higher magnification of different positions at the CML between two sclereids showing the pit pair structure. The dashed white area is the sclereid and the dashed blue lines are trumpet-shaped junctions. The pit pair structure at the CML shows a symmetrical trumpet-shaped junction with a pit membrane.

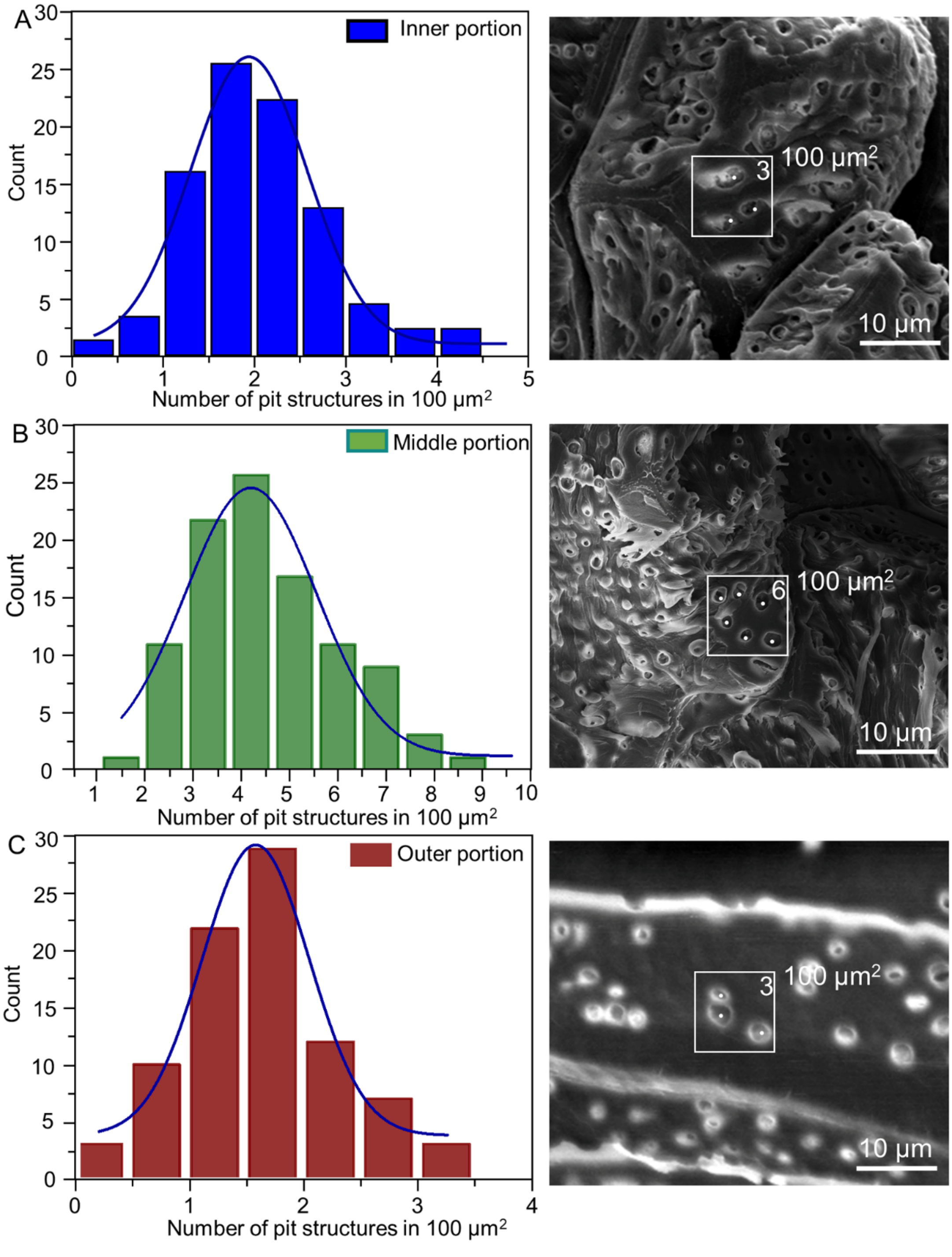


**Fig. S11. The statistical data of the pit structure.**
The average number of pit structures in 100 μm$^2$ of in the inner portion (**A**), the middle portion (**B**) and the outer portion (**C**) is 1-3, 3-5, and 1-3, respectively. The SEM image shows a corresponding region with an area of 100 μm$^2$ and the pits in this region, which are illustrated by white dots.

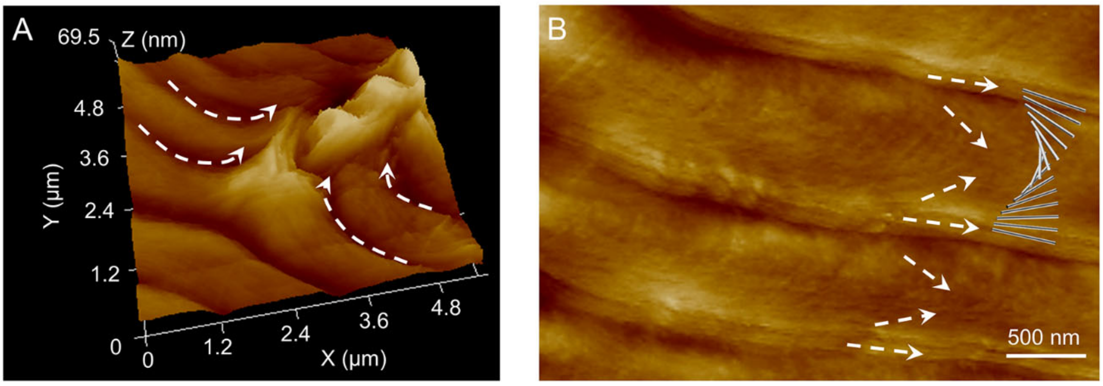


**Fig. S12. AFM images of the alignment of the cell walls.**

AFM images of the alignment of the cell walls around a pit (**A**) and the cell wall with the helicoidal pattern (**B**).

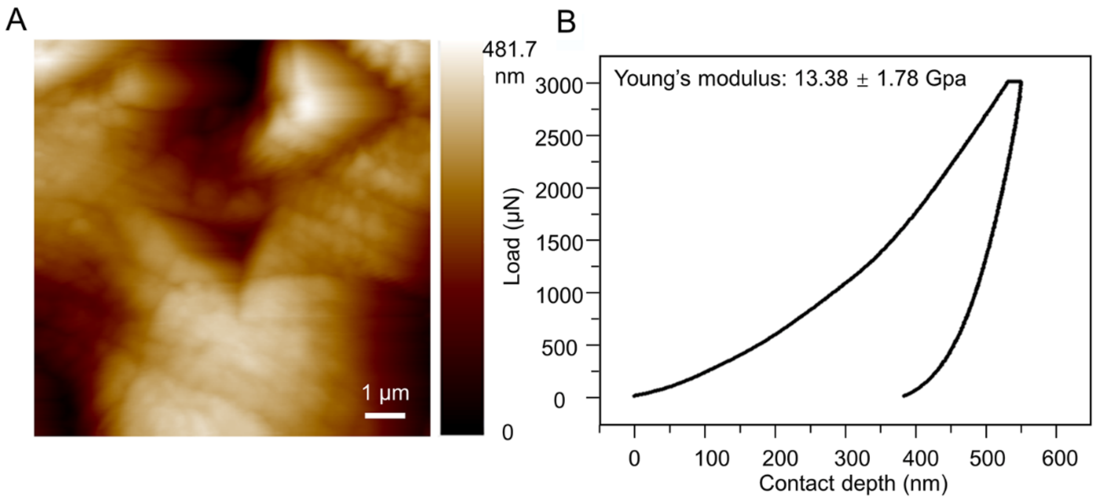


**Fig. S13. Nanoindentation test of the ginkgo seed shell.**

(**A**) AFM image of the cross section of ginkgo seed shell after a nanoindentation test. The indentation made by the diamond Berkovich tip can be clearly observed. (**B**) The corresponding nanoindentation loading-unloading curve. The modulus was calculated from the loading-unloading curve with an average value of 13.38 ± 1.78 GPa.

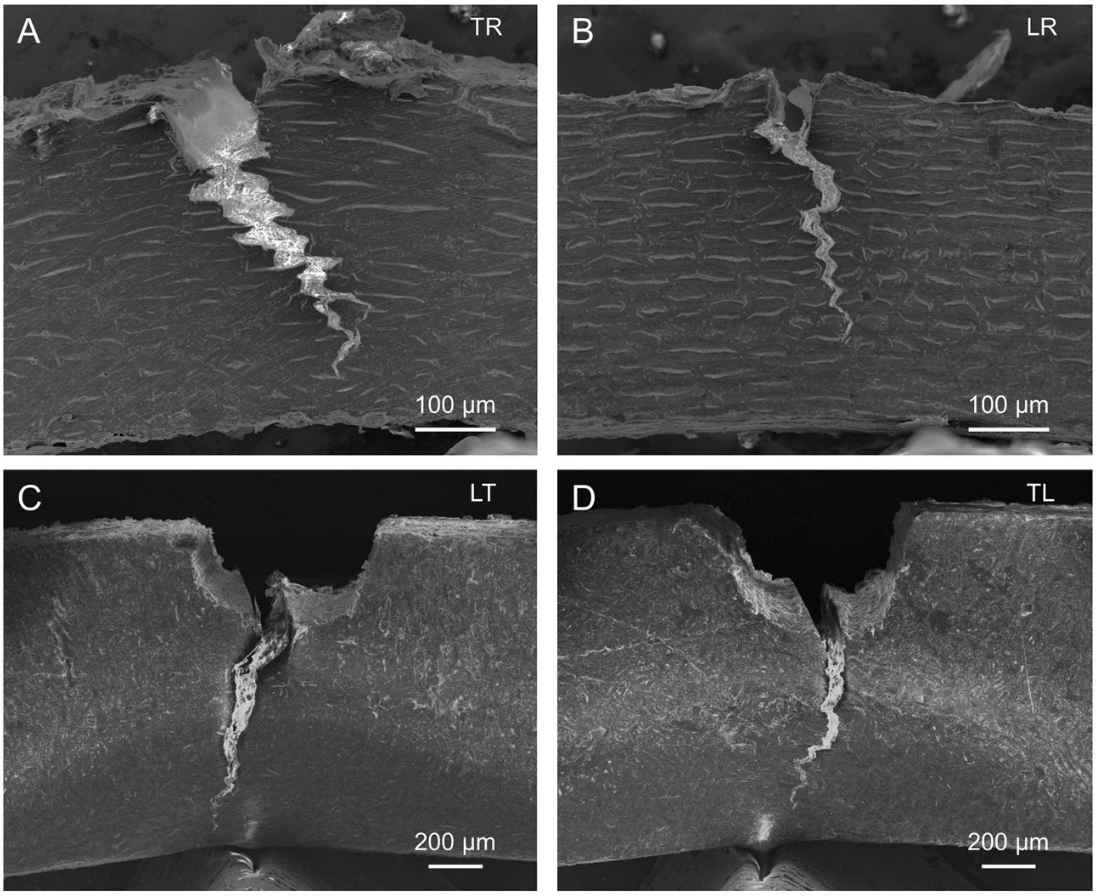


**Fig. S14. The crack paths for the four propagation directions.**

The crack paths for the four propagation directions: TR (**A**), LR (**B**), LT (**C**), and TL (**D**). The fracture cracks in these four directions all exhibit complex toughening mechanisms, such as crack deflection and branching. The crack propagation for TR shows a more efficient crack resistance with more "zig-zag" crack wake.

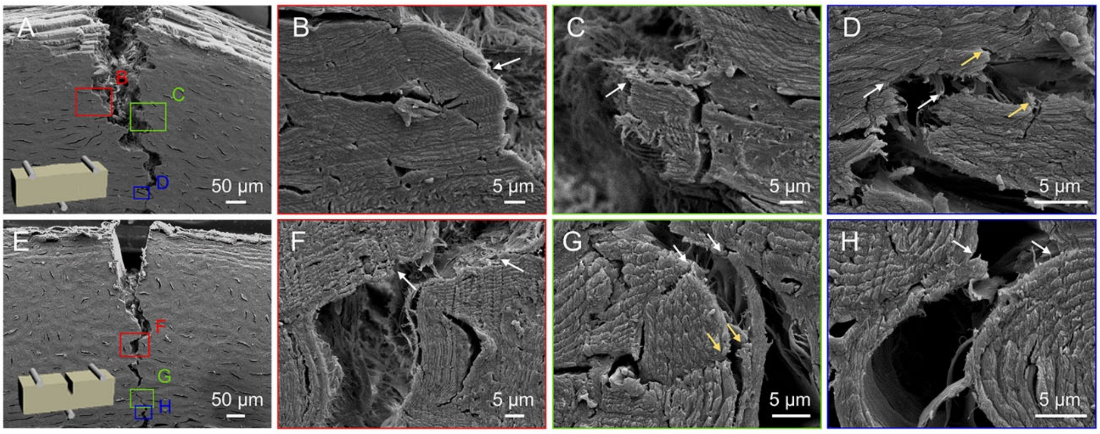


**Fig. S15. In-situ SEM images of the crack propagation.**

In-situ SEM images of the crack propagation of an unnotched sample (**A**) and a single-edge notched sample (**E**) of the ginkgo seed shell after three-point bend testing. Detailed morphologies (**B**, **C**, **D**) for the unnotched sample and (**F**, **G**, **H**) for the notched sample. The unnotched sample shows the cleavage (B) and breakage (C, D) of the sclereids. The crack can be terminated by the cell cavity and deflected along other directions (D). The white arrows (in B, C, D) illustrate the pits, which act as the entrances to guide the crack into the sclereid. Compared with the notched sample (F–H), the crack propagation shows no significant distinction. Arrows of the same color indicate the same pair of pits that has been broken.

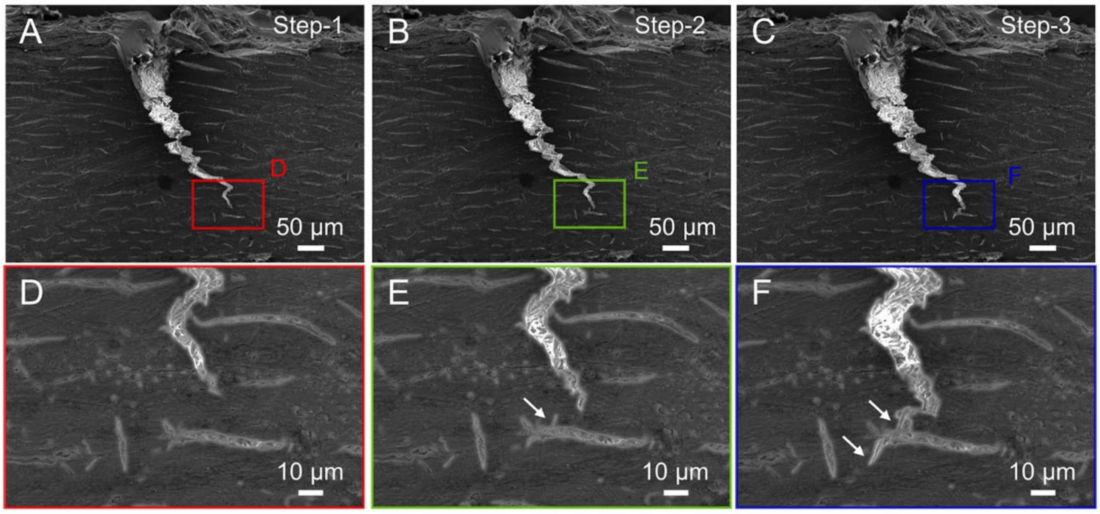


**Fig. S16. SEM images of the crack propagation at the single-edge notched sample.**
In-situ SEM images of the crack propagation at the single-edge notched sample of ginkgo seed shell (**A**–**C**) with corresponding high-magnification images (**D**–**F**), showing the clear initiation of the crack propagating into the sclereid through the pit structure. The pit structure within the sclereid is identified by the white arrow.

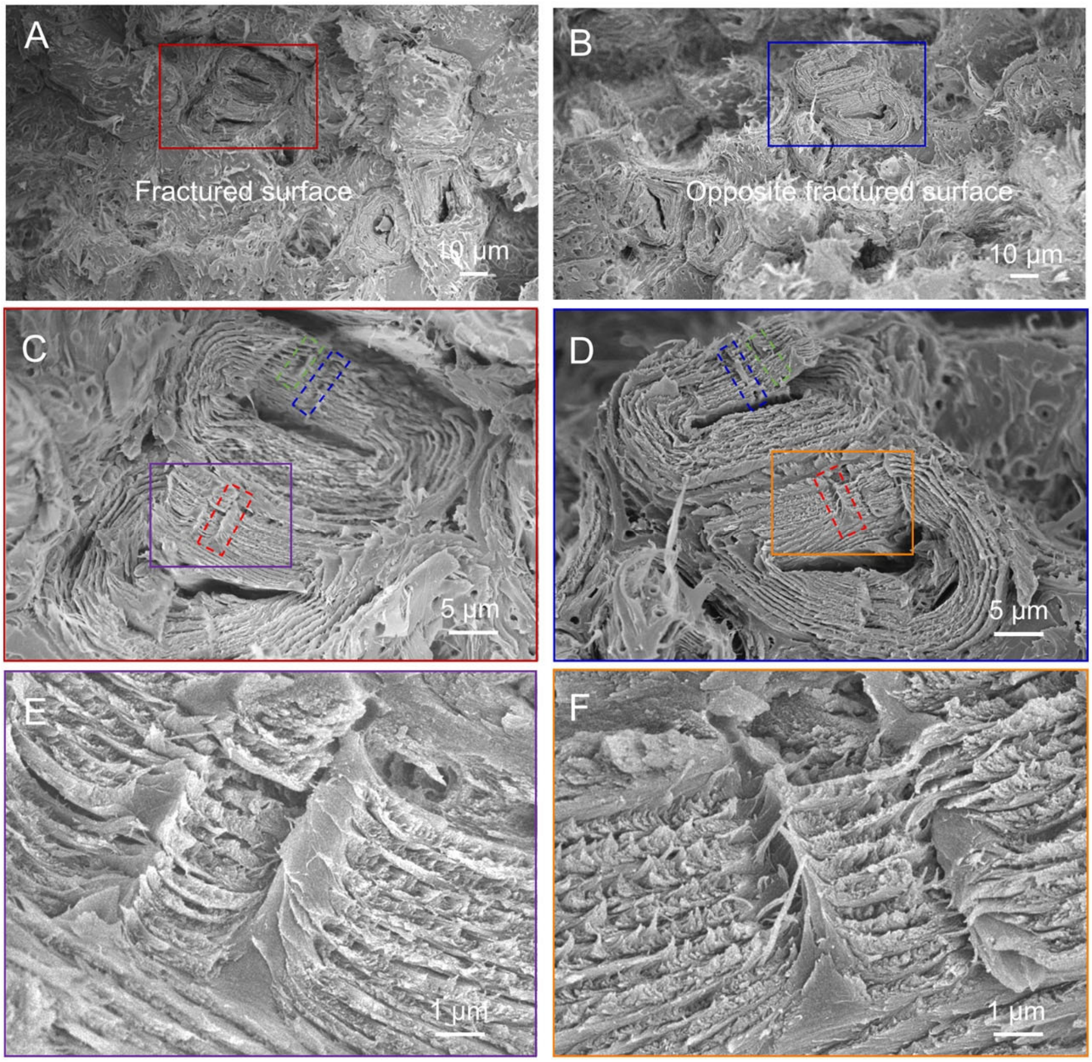


**Fig. S17. SEM images of two separated sclereids showing the "stretched pits" in dry state.** SEM images of the fractured surface (**A**) and the opposite fractured surface (**B**) from a sample in dry state. SEM images of pits guiding the fracture through the cells (**C**) and through broken cells left behind on the opposite fracture surface (**D**). (**E** and **F**) The "pulled-out" pits on the surface of a fractured cell and left "hole". The dashed red, blue and green areas in (c and d) are pits divided into two parts.

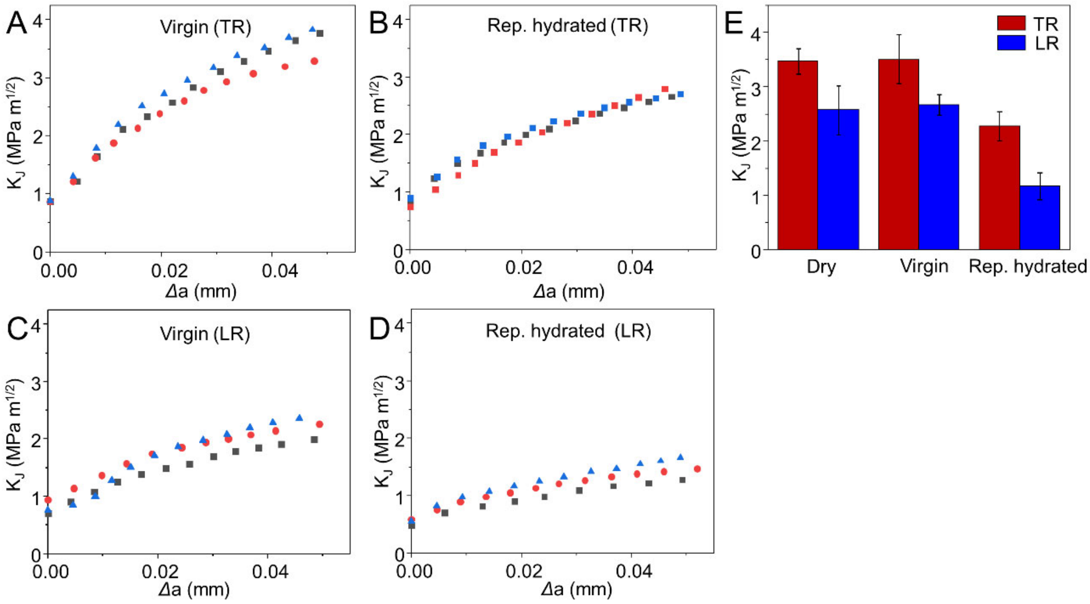


**Fig. S18. The rising resistance R-curves for the cracks in different hydrated states.**
The rising resistance R-curves for the cracks in virgin state TR direction (**A**), repeatedly hydrated (Rep. hydrated) state TR direction (**B**), virgin state LR direction (**C**), and Rep. hydrated LR direction (**D**). (**E**) The $K_{JC}$ for the two crack orientations with different moisture content ($\Delta a \approx 0.05$ mm).

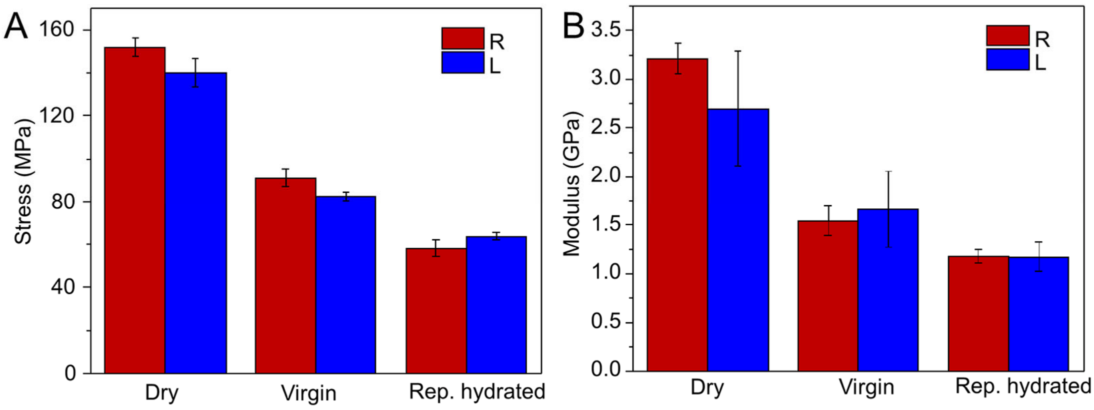


**Fig. S19. The ultimate tensile stress and tensile modulus of seed shells in different hydrated states.**

(**A**) The ultimate tensile stress of seed shells in dry, virgin and repeatedly hydrated (Rep, hydrated) state parallel (R) to and perpendicular (L) to equator direction. (**B**) Tensile modulus obtained from the stress-strain curves.

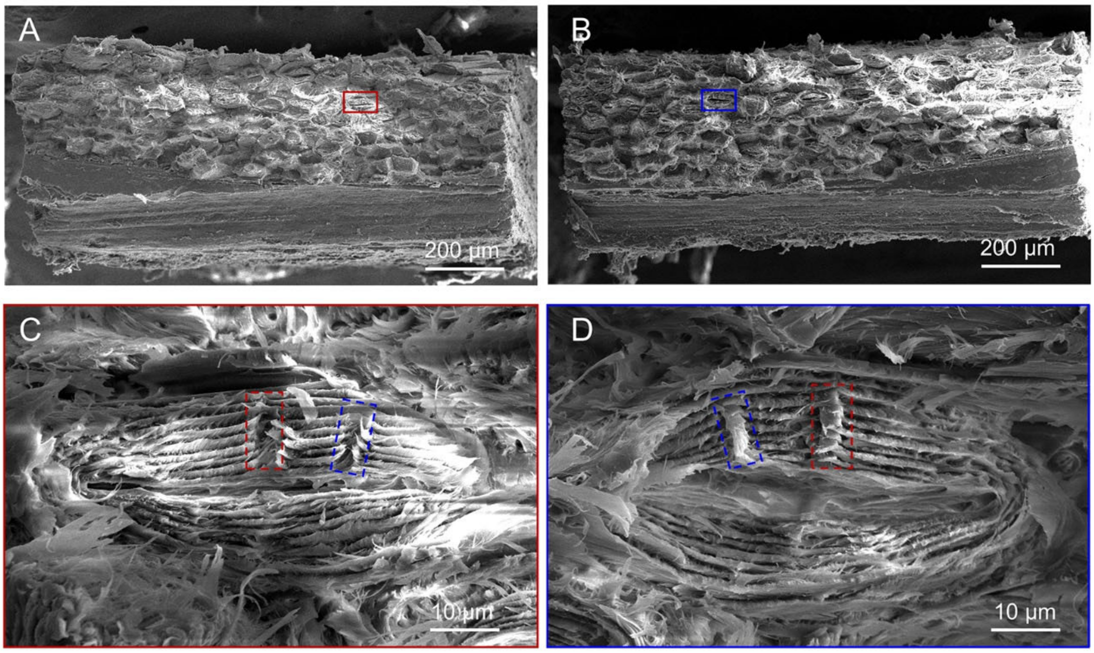


**Fig. S20. SEM images of the two fractured surfaces from one sample in virgin state.**
SEM images of the fractured surface (**A**) and the opposite fractured surface (**B**) from a sample in virgin state. SEM images of pits guiding the fracture through the cells (**C**) and through broken cells (**D**) left behind on the opposite fracture surface. The dashed red and blue areas in (c and d) are pits divided into two parts.

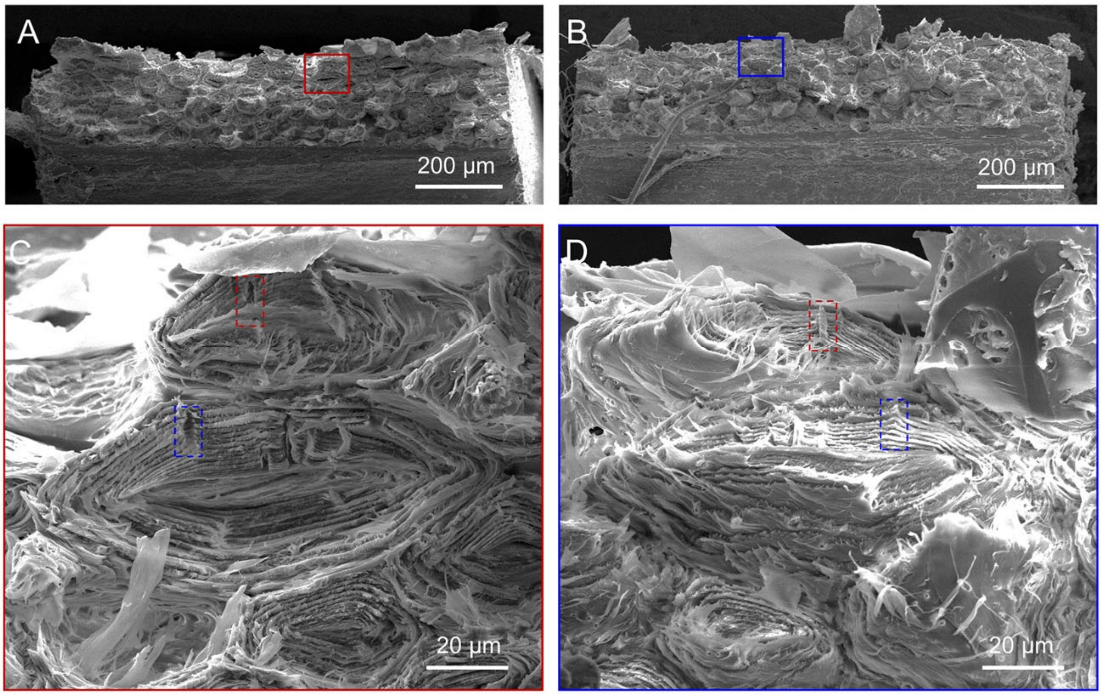


**Fig. S21. SEM images of the two fractured surfaces from one sample in repeatedly hydrated state.**

SEM images of the fractured surface (**A**) and the opposite fractured surface (**B**) from a sample in repeatedly hydrated state. SEM images of pits guiding the fracture through the cells (**C**) and (**D**) the opposite fracture surface. The dashed red and blue areas in (c and d) are pits divided into two parts.

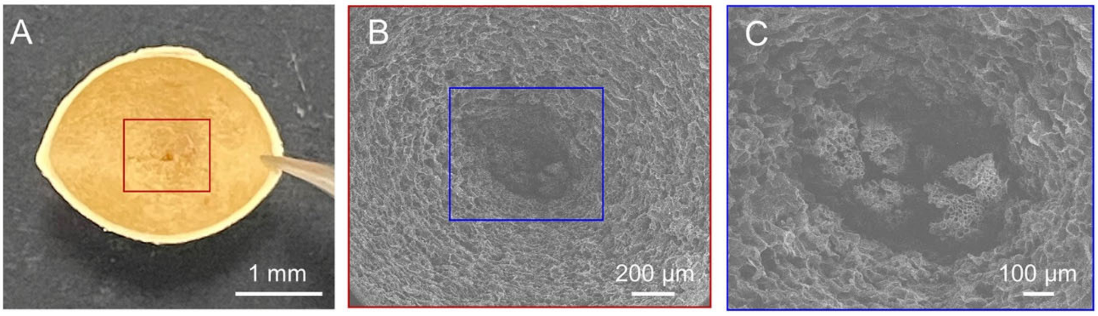


**Fig. S22. Digital and SEM images of a hole at the end of seed shell.**
(**A**) The digital image of one end of the ginkgo seed shell. (**B**) SEM image of a hole at one end of the shell while it is dormant and (**C**) magnified images of the hole.

**Table S1. Young's modulus of ginkgo seed shell obtained from the nanoindentation measurements with different water content.**

The dry seed shell sample is a piece with a length of 8 mm, width of 5 mm, and thickness of 0.6 mm. After the nanoindentation test, the sample was immersed in deionized water for 30 minutes, then dried in ambient air for 17, 27, 40, and 60 min, respectively. These samples are designated I, II, III, and IV. The water content of each sample was measured by thermogravimetric analysis.

| Sample | Young's modulus (GPa) | Water content (%) |
|---|---|---|
| Dry | 10.80 | 5.64 |
| I | 3.91 | 8.19 |
| II | 6.55 | 7.44 |
| III | 6.87 | 7.10 |
| IV | 8.96 | 6.18 |

**Movie S1.** 3D reconstruction of the sclereids using synchrotron X-ray micro-CT.

**Movie S2.** In-situ SEM characterization of the crack entering into a sclereid guided by the pit.

## SI References


1. C. Chen. Stress intensity factor of three-point bending fracture toughness specimen. *Chin. J. Theor. Appl. Mech.* **10**, 121–124 (1974).
2. X. D. Li, B. Bhushan. A review of nanoindentation continuous stiffness measurement technique and its applications. *Mater. Charact.* **48**, 11-36 (2002).
3. J. J. Vlassak, M. Ciavarella, J. R. Barber, X. Wang. The indentation modulus of elastically anisotropic materials for indenters of arbitrary shape. *J. Mech. Phys. Solids* **51**, 1701-1721 (2003).
4. J. G. Swadener, G. M. Pharr. Indentation of elastically anisotropic half-spaces by cones and parabolae of revolution. *Philos. Mag. A* **81**, 447-466 (2001).
5. W. C. Oliver, G. M. Pharr. Measurement of hardness and elastic modulus by instrumented indentation: Advances in understanding and refinements to methodology. *J. Mater. Res.* **19**, 3-20 (2004).
6. D. M. Barnett, J. Lothe. Line force loadings on anisotropic half-spaces and wedges. *Phys. Norv.* **8,** 13–22 (1975).
7. J. R. Barber. Determining the contact area in elastic-indentation problems. *J. Strain Anal. Eng. Des.* **9,** 230–232 (1974).